

Spontaneous emission spectra and quantum light-matter interactions from a strongly coupled quantum dot metal-nanoparticle system

C. Van Vlack,^{1,*} Philip Trøst Kristensen,² and S. Hughes¹¹Queen's University, Department of Physics, Kingston Ontario, Canada K7L 3N6²DTU Fotonik, Technical University of Denmark, 2800 Kgs. Lyngby, Denmark

(Received 22 December 2011; revised manuscript received 10 January 2012; published 3 February 2012)

We investigate the quantum optical properties of a quantum-dot dipole emitter coupled to a finite-size metal nanoparticle using a photon Green-function technique that rigorously quantizes the electromagnetic fields. We first obtain pronounced Purcell factors and photonic Lamb shifts for both a 7- and 20-nm-radius metal nanoparticle, without adopting a dipole approximation. We then consider a quantum-dot photon emitter positioned sufficiently near the metal nanoparticle so that the strong-coupling regime is possible. Accounting for nondipole interactions, quenching, and photon transport from the dot to the detector, we demonstrate that the strong-coupling regime should be observable in the far-field spontaneous emission spectrum, even at room temperature. The vacuum-induced emission spectra show that the usual vacuum Rabi doublet becomes a rich spectral triplet or quartet with two of the four peaks anticrossing, which survives in spite of significant nonradiative decays. We discuss the emitted light spectrum and the effects of quenching for two different dipole polarizations.

DOI: [10.1103/PhysRevB.85.075303](https://doi.org/10.1103/PhysRevB.85.075303)

PACS number(s): 42.50.Pq, 78.67.Bf, 73.20.Mf

I. INTRODUCTION

The route to photonic vacuum engineering traditionally employs a lossless dielectric cavity system, exploiting an optical mode with a suitably large quality factor Q and small effective mode volume V . The local photon density of states (LDOS) scales proportionally with the Q/V factor. Enhancing the LDOS through the use of small cavities¹ has shown to be a very effective method for increasing the radiative decay rate of an emitter via the Purcell effect.² In solid-state materials, cavities are created using various structural designs, including photonic crystal lattices with defects,³ and etched micropillars made of Bragg reflectors.⁴ These dielectric cavities have shown some remarkable successes in quantum optics, but the lower limit on V in such systems is typically set by diffraction, with $V \approx (\lambda/n)^3$, where n is the refractive index of the cavity. Additionally, when one uses semiconductor quantum dots (QDs), the narrow-band resonance associated with high Q requires very long nonradiative exciton decay times, only achievable at low temperatures.

In an effort to further increase the LDOS and decrease the system size to subwavelength dimensions, it can be advantageous to examine plasmonic systems where light is confined to the surface of a metal and decays evanescently from its surface. For example, a metal nanoparticle (MNP) supports localized surface plasmons (LSPs)⁵ that are tightly confined spatially and not limited by diffraction. This allows coupling between single-photon emitters and MNPs,⁶ which can enhance the LDOS in a system as small as 10–20 nm³. When the LDOS becomes large enough, it may also be possible to enter the *strong-coupling* regime where instead of the irreversible process of the emitter decaying and emitting a photon into the environment (i.e., weak coupling), the emitter can *reversibly* exchange the photon with the environment—resulting in vacuum Rabi oscillations. In order for this to happen, the coupling between the emitter and the environment must exceed all possible decay channels. Classical predictions of strong-coupling behavior have been made in the context of

metallic dimers,⁷ though it is not known if the splitting survives in the observable spontaneous (i.e., vacuum-induced) emission spectrum. This reversible exchange of energy is fundamentally interesting and can possibly be useful for applications in coherent control,⁸ quantum information processing,⁹ and lasing/spasing.^{10–12} With regard to a quantum theory of the light-matter processes in the strong-coupling regime, several complications arise in the theoretical description of coupling quantized light to a MNP, including the need to quantize the fields in a dissipative/lossy medium. Waks and Sridharan¹³ introduced a useful quantized cavity-QED (quantum electrodynamics) treatment of a coupled MNP and a dipole emitter (e.g., a QD), with the MNP treated within the dipole approximation;¹⁴ however, it is known that the dipole approximation can yield poor agreement with exact (i.e., nondipole) calculations obtained from finite-size MNPs—unless placed at least a few radii from the MNP surface.^{15–17} Trügler and Hohenester¹⁸ have examined the strong-coupling dynamics between a molecule and a cigar-shaped MNP employing a mode expansion technique, which incorporates the higher order plasmon modes; their quantum approach assumes a Lorentzian form for the broadening of the modes, via Lindblad superoperators in a master-equation formalism;^{19,20} this useful nondipole study predicts that the strong-coupling regime is possible between a MNP and a molecule, though there is no direct connection to the emission spectrum. For dielectric cavity systems, the effects of propagation to a detector is generally assumed to not change the spectral shape of the emitted photons. However, for a metallic system, because of the losses associated with the MNP and quenching, it is essential to compute the generalized light spectrum (i.e., away from the QD position) to first realize if the strong-coupling effects are observable, and second, to see how the spectral signatures may change and how they would be measured.

In this work, we develop a theoretical formalism that allows one to obtain the emission spectra at any spatial position of the detector. In Sec. II, we describe an exact medium-independent quantum optics approach—formulated in terms of photonic

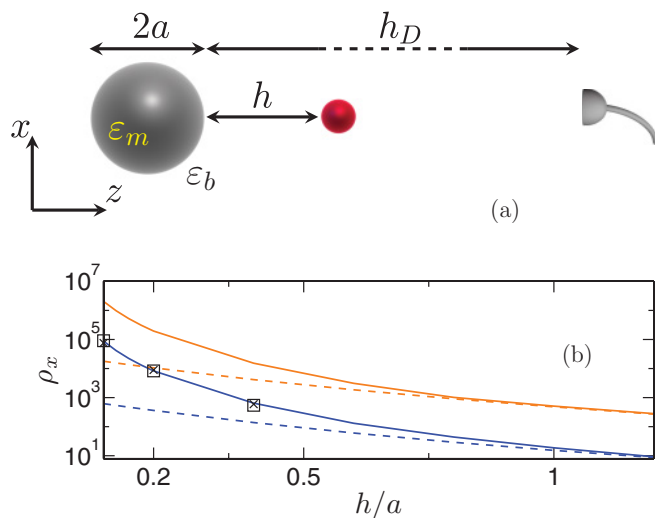


FIG. 1. (Color online) (a) Schematic of the MNP embedded in a background material with permittivity of ϵ_b . The MNP, with radius a and permittivity ϵ_m , is located at the origin. The single photon emitter (QD) at \mathbf{r}_d is located at height h above the surface of the MNP. We also consider a pointlike detector at \mathbf{r}_D located along the same axis at height h_D above the metal surface. (b) LDOS peak as a function of height above a 20-nm (blue-dark) and 7-nm (orange-light) spherical silver MNP for an x -oriented dipole. The nondipole result (for the MNP) is given by the solid line and the dipole-approximation result is given by the dashed line. For comparison, using the 20-nm MNP, selected FDTD results are shown as squares (1-nm grid) and crosses (2-nm grid), showing very good agreement for different effective emitter sizes.

Green functions—to describe the cavity-QED interactions and photon transport between a dipole emitter (QD), a finite-size MNP, and a detector. A schematic of the nanoscale interaction geometry is shown in Fig. 1(a). In Sec. III, we present various numerical results and calculations for the coupled QD-MNP system. We first calculate the classical Green function above a MNP using a well established scattering approach,^{21,22} and subsequently calculate the LDOS and photonic Lamb shift from a nearby dipole emitter, using two different sized MNPs (7 and 20 nm radius). We find significant enhancements in the LDOS near the MNP surface¹⁶ and simultaneously observe enormous Lamb shifts. We then examine the spectral properties of a QD dipole emitter in the strong-coupling regime. We compute the far-field spontaneous emission spectrum, fully accounting for non-Markovian relaxation and propagation effects to the detector. The spontaneous emission spectrum is shown to yield clear signatures of the strong-coupling regime, but is found to be much richer than the usual vacuum Rabi splitting known from simpler cavity-QED systems (e.g., using dielectric cavities) due to the interplay between higher-order mode coupling and dipolar-mode coupling; the non-Markovian spectra yield a spectral triplet or even a quartet of resonances, where two of the peaks anticross, thus signaling the strong-coupling regime. We present the strong-coupling spectra for two different QD-dipole polarizations and discuss the effects of optical quenching. In Sec. IV, we give a brief discussion about possible experimental configurations for observing our predictions, and in Sec. V we conclude.

II. THEORY

A. Green function of a spherical metal nanoparticle

The classical photon Green function in a medium with $\epsilon(\mathbf{r}, \omega)$ (complex dielectric constant) and $\mu = 1$ is described through the following equation:

$$\nabla \times \nabla \times \mathbf{G}(\mathbf{r}, \mathbf{r}'; \omega) - \epsilon(\mathbf{r}, \omega) k_0^2 \mathbf{G}(\mathbf{r}, \mathbf{r}'; \omega) = k_0^2 \delta(\mathbf{r} - \mathbf{r}'), \quad (1)$$

where $k_0 = \omega/c$, ω is the angular frequency and c is the speed of light. The dipole-response function (Green function) \mathbf{G} can connect to both classical and quantum light-matter interactions. For the MNP problem of interest, we will discuss the Green function within and outside the dipole approximation. Typically for small MNPs ($\omega \sqrt{\epsilon_b} a / c \ll 1$) of permittivity ϵ_m embedded in a material with permittivity ϵ_b , the Green function is obtained through the Dyson equation where we assume that the spherical MNP response can be modelled through the metal polarizability function:

$$\alpha_m(\omega) = \frac{\alpha_m^0(\omega)}{\left[1 - \frac{i\alpha_m^0 \omega^3 \sqrt{\epsilon_b}}{6\pi c^3 a^3}\right]}, \quad (2)$$

with the bare polarizability (i.e., without photon coupling to the environment)

$$\alpha_m^0(\omega) = 4\pi \epsilon_b a^3 \frac{(\epsilon_m(\omega) - \epsilon_b)}{[\epsilon_m(\omega) + 2\epsilon_b]}, \quad (3)$$

and Eq. (2) also accounts for *radiation reaction*.²³ Considering the MNP to be located at position \mathbf{r}_m , then the MNP-dipole Green function is obtained through^{24,25}

$$\mathbf{G}(\mathbf{r}, \mathbf{r}') = \mathbf{G}_0(\mathbf{r}, \mathbf{r}') + \mathbf{G}_0(\mathbf{r}, \mathbf{r}_m) \cdot \alpha_m \mathbf{G}_0(\mathbf{r}_m, \mathbf{r}'). \quad (4)$$

To account for the finite-size nature of the MNP, we also compute the Green function outside the dipole approximation. For these calculations we use an established analytical approach where the Green function is expanded in spherical vector functions and the boundary conditions are satisfied at the edge of the sphere;^{21,22} we relegate the details of this approach to the Appendix.

B. Classical light-matter interactions

An integral solution for the classical electric field can be written as

$$\mathbf{E}(\mathbf{r}, \omega) = \mathbf{E}^0(\mathbf{r}, \omega) + \int d\mathbf{r}' \mathbf{G}(\mathbf{r}, \mathbf{r}'; \omega) \cdot \mathbf{P}(\mathbf{r}', \omega), \quad (5)$$

where \mathbf{P} is a polarization source. As we will show below, in quantum optics, the \mathbf{E} and \mathbf{P} fields become operators, but \mathbf{G} remains the same.^{26,27} For a dipole emitter at position \mathbf{r}_d , $\mathbf{E}(\mathbf{r}) = \mathbf{E}^0(\mathbf{r}) + \mathbf{G}(\mathbf{r}, \mathbf{r}_d) \cdot \alpha_d \mathbf{E}(\mathbf{r}_d)$, where the dipole polarizability of the QD exciton is given by

$$\alpha_d(\omega) = \frac{2\omega_d d^2 / \hbar \epsilon_0}{(\omega_d^2 - \omega^2 - i\gamma_d \omega) \hbar \epsilon_0}, \quad (6)$$

with ω_d the transition frequency, γ_d the nonradiative broadening of the QD exciton, d the optical dipole moment, \hbar the reduced Planck constant, and ϵ_0 the permittivity of free space. Assuming a QD dipole of the form $\mathbf{d} = d\mathbf{n}_i$, the (*projected*) LDOS becomes

$$\rho_i(\mathbf{r}_d; \omega) = \frac{\text{Im}[\mathbf{n}_i \cdot \mathbf{G}(\mathbf{r}_d, \mathbf{r}_d; \omega) \cdot \mathbf{n}_i]}{G_{\text{hom}}}, \quad (7)$$

where $G_{\text{hom}} = \text{Im}[\mathbf{n}_i \cdot \mathbf{G}_{\text{hom}}(\mathbf{r}, \mathbf{r}; \omega) \cdot \mathbf{n}_i] = k_0^3 \sqrt{\epsilon_b} / 6\pi$, and \mathbf{G}_{hom} is the homogeneous-medium Green function. The units of Eq. (7) are conveniently chosen so that the LDOS is equal to the Purcell factor,² which describes—in a *weak-coupling regime*—the spontaneous (vacuum-induced) emission rate,

$$\gamma_{\text{EM}}(\mathbf{r}_d; \omega) = \frac{2d^2 \rho(\mathbf{r}_d; \omega) G_{\text{hom}}}{\hbar \epsilon_0}. \quad (8)$$

This total electromagnetic (EM) decay rate includes both radiative and nonradiative coupling with the lossy environment, and it depends on the \mathbf{G} of the medium. In order to describe photon propagation from the QD to a detector (e.g., to the far field), we also consider the nonlocal propagator, which is defined through the two space-point Green function,

$$\rho_{ij}^{\text{nl}}(\mathbf{r}, \mathbf{r}'; \omega) = \frac{[\mathbf{n}_i \cdot \mathbf{G}(\mathbf{r}, \mathbf{r}'; \omega) \cdot \mathbf{n}_j]}{G_{\text{hom}}}. \quad (9)$$

$$\rho(\mathbf{r}_d, \omega) = \frac{\int_{V_{\text{QD}}} d\mathbf{r} F_e(\mathbf{r}) F_h(\mathbf{r}) \int_{V_{\text{QD}}} d\mathbf{r}' F_e^*(\mathbf{r}') F_h^*(\mathbf{r}') \text{Im}[\mathbf{n}_i \cdot \mathbf{G}(\mathbf{r}, \mathbf{r}'; \omega) \cdot \mathbf{n}_i]}{\int_{V_{\text{QD}}} d\mathbf{r} F_e(\mathbf{r}) F_h(\mathbf{r}) \int_{V_{\text{QD}}} d\mathbf{r}' F_e^*(\mathbf{r}') F_h^*(\mathbf{r}') \text{Im}[\mathbf{n}_i \cdot \mathbf{G}_{\text{hom}}(\mathbf{r}, \mathbf{r}'; \omega) \cdot \mathbf{n}_i]}, \quad (11)$$

where $F_e(\mathbf{r})/F_h(\mathbf{r})$ are the ground-state electron/hole wave functions (centred at \mathbf{r}_d), and V_{QD} is the volume of the QD. For strongly confined QDs, the effects of treating the QD in the dipole approximation is to reduce/enhance the effective dipole moment of the QD.³⁰ To investigate the effects of averaging over a $(2\text{ nm})^3$ volume, we compared finite-difference time-domain (FDTD) results for different griddings near the MNP and observe excellent agreement between grids of 1 nm and 2 nm and the analytic Green function described in the Appendix [see Fig. 1(b)]. Such an agreement means that the field averaging across an FDTD unit cell is sufficient at these heights implying that the average field across a QD of the same approximate size is valid. This has been further verified by independent calculations examining local-field effects inside lossy structures and comparing with the exact integration of the Green function³² (i.e., the regularized Green function) over a unit cell of the same size (which we will discuss in more detail in future work). Additionally, for strongly confined dots, then the higher-lying energy levels become increasingly separated further justifying the dipole approximation for a single QD transition.³³ It is possible that the QD response may be influenced by higher-order QD mode contributions, but due to the size of the dots compared to the MNPs we expect such contributions to be small and, to simplify the calculations, we will ignore them. Any further references to

The photonic (or *anomalous*) Lamb shift is also connected to the Green function, and is obtained from^{26,28}

$$\Delta\omega_i(\mathbf{r}_d; \omega) = -\frac{d^2 \text{Re}[\mathbf{n}_i \cdot \mathbf{G}(\mathbf{r}_d, \mathbf{r}_d; \omega) \cdot \mathbf{n}_i]}{\hbar \epsilon_0}. \quad (10)$$

For the Green function used in Eq. (10), i.e., with the same two spatial arguments $\text{Re}[\mathbf{G}(\mathbf{r}, \mathbf{r})]$, we will neglect the (divergent) homogeneous-medium contribution since its effect can be absorbed into the definition of ω_d .^{25,29}

The quantities introduced above (e.g., the photon decay rate and the Lamb shift) are well known, and are perturbative in nature (in their definition). However, this is not a model restriction. Indeed, the theory above can fully include nonperturbative light-matter interactions. To reach the *strong-coupling regime* of cavity QED, where light-matter interactions must be included to all orders, one requires the dipole-medium coupling rate g to be larger than any dissipation channels.^{7,18} For a single *quasimode* of the MNP, e.g., $\mathbf{f}_m(\mathbf{r})$, then $g \equiv g_m = \sqrt{\omega_m / 2\hbar \epsilon_0} \mathbf{d} \cdot \mathbf{f}_m(\mathbf{r}_d)$ so that the vacuum Rabi splitting, $2g \approx \sqrt{\gamma_{\text{EM}}(\rho) \gamma_{\text{LSP}} / 2} \gg \gamma_d, \gamma_{\text{LSP}}$. Here $\gamma_{\text{EM}}(\rho)$ accounts for all EM decay processes and γ_{LSP} is the effective linewidth of the LSP dipole mode; for the purpose of the scaling argument above, we are also tacitly assuming a Lorentzian line shape for $\rho(\omega)$.

Since we are investigating nondipolar effects for the MNP, it is worth discussing nondipolar effects for the QD as well. The generalization of Eq. (7) to include nondipole effects is given by the following formula:^{30,31}

the dipole approximation will refer to the MNP and the QD will always be assumed to be in the dipole approximation. For now, we highlight that our general approach can include nondipole effects for the QD using the same Green functions introduced above.

C. Quantum light-matter interactions and the emission spectrum

To describe the quantum light-matter interaction, we adopt a medium-dependent quantization procedure for calculating the emission spectrum from a two-level system (exciton) in a lossy, nonhomogeneous environment.^{26,27} We begin with the complete Hamiltonian of the coupled system,

$$H = \hbar \omega_d \hat{\sigma}^+ \hat{\sigma}^- + \hbar \int d\mathbf{r} \int_0^\infty d\omega_l \omega_l \hat{\mathbf{f}}^\dagger(\mathbf{r}, \omega_l) \cdot \hat{\mathbf{f}}(\mathbf{r}, \omega_l) - [\hat{\sigma}^+ \mathbf{d} + \hat{\sigma}^- \mathbf{d}] \cdot \hat{\mathbf{E}}(\mathbf{r}_d), \quad (12)$$

where $\hat{\sigma}^+, \hat{\sigma}^-$ are the Pauli operators of the QD exciton (located at position \mathbf{r}_d), $\hat{\mathbf{f}}^\dagger/\hat{\mathbf{f}}$ are the bosonic continuum field creation/annihilation operators of the total electric-field operator (including interactions with the QD), which are indexed in the Hamiltonian with continuous eigenfrequencies

ω_l , and the dipole \mathbf{d} is assumed to be real. The electric-field operator is related to the bosonic field operators through²⁸

$$\hat{\mathbf{E}}(\mathbf{r}, t) = \hat{\mathbf{E}}^0(\mathbf{r}, t) + i \sqrt{\frac{\hbar}{\pi \epsilon_0}} \int_0^\infty d\omega_l \int d\mathbf{r}' \mathbf{G}(\mathbf{r}, \mathbf{r}'; \omega_l) \cdot \sqrt{\epsilon_I(\mathbf{r}', \omega_l)} \hat{\mathbf{f}}(\mathbf{r}', \omega_l; t) + \text{H.c.}, \quad (13)$$

where ϵ_I is the imaginary part of the permittivity and $\hat{\mathbf{E}}^0(\mathbf{r}, t)$ is the *free field*, i.e., the field that exists without the presence of the QD. To proceed we will adopt the weak excitation approximation, so that we assume at most one excitation in the system (this approximation is exact when the initial field is the vacuum field). Using the Heisenberg equations of motion, and Laplace transforming to the spectral domain, we can subsequently obtain explicit expressions for $\hat{\sigma}^+$, $\hat{\sigma}^-$ and $\hat{\mathbf{f}}, \hat{\mathbf{f}}^\dagger$. The total electric-field operator is then²⁶

$$\begin{aligned} \hat{\mathbf{E}}(\mathbf{r}, \omega) &= \hat{\mathbf{E}}^0(\mathbf{r}, \omega) + \int \frac{\text{Im} \mathbf{G}(\mathbf{r}, \mathbf{r}_d; \omega_l) \cdot \mathbf{d}}{\pi \epsilon_0} \frac{\hat{\sigma}^-(\omega) + \hat{\sigma}^+(\omega)}{\omega - \omega_l}, \\ &= \hat{\mathbf{E}}^0(\mathbf{r}, \omega) + \frac{1}{\epsilon_0} \mathbf{G}(\mathbf{r}, \mathbf{r}_d; \omega) \cdot \mathbf{d} [\hat{\sigma}^-(\omega) + \hat{\sigma}^+(\omega)], \end{aligned} \quad (14)$$

in which we have used the relation $\frac{i}{\omega_l - \omega + i\epsilon_+} = \pi \delta(\omega_l - \omega) + iP(\frac{1}{\omega_l - \omega})$, with P the principle value. The sum of the dipole operators are given by

$$\begin{aligned} &\hat{\sigma}^-(\omega) + \hat{\sigma}^+(\omega) \\ &= \frac{-i[\hat{\sigma}^-(t=0)(\omega + \omega_d) + \hat{\sigma}^+(t=0)(\omega - \omega_d)]}{\omega_d^2 - \omega^2 - 2\omega_d \mathbf{d} \cdot \mathbf{G}(\mathbf{r}_d, \mathbf{r}_d; \omega) \cdot \mathbf{d} / \hbar \epsilon_0}. \end{aligned} \quad (15)$$

The light spectrum is defined through $S(\mathbf{r}, \omega) = \int_0^\infty dt_1 \int_0^\infty dt_2 e^{i\omega(t_2 - t_1)} \langle [\hat{\mathbf{E}}(\mathbf{r}, t_1)]^\dagger \hat{\mathbf{E}}(\mathbf{r}, t_2) \rangle$, which gives $S(\mathbf{r}, \omega) = \langle [\hat{\mathbf{E}}(\mathbf{r}, \omega)]^\dagger \hat{\mathbf{E}}(\mathbf{r}, \omega) \rangle$. For $\mathbf{r} = \mathbf{r}_D$, and assuming an initially excited QD exciton in vacuum, one obtains²⁶ the emitted light-spectrum, analytically,

$$S(\mathbf{r}_D, \omega) = \left| \frac{\mathbf{d} \cdot \mathbf{G}(\mathbf{r}_D, \mathbf{r}_d; \omega)(\omega + \omega_d) / \epsilon_0}{\omega_d^2 - \omega^2 - i\omega\gamma_d - 2\omega_d \mathbf{d} \cdot \mathbf{G}(\mathbf{r}_d, \mathbf{r}_d; \omega) \cdot \mathbf{d} / \hbar \epsilon_0} \right|^2, \quad (16)$$

where the point detector is assumed to be at position \mathbf{r}_D above the center of the MNP. We highlight that this final spectrum is exact in both weak- and strong-coupling limits. In order to more clearly extract the physics associated with propagation and quenching, we will also examine the dipole or polarization spectrum:

$$\begin{aligned} P(\omega) &\equiv \langle \hat{\sigma}^+(\omega) \hat{\sigma}^-(\omega) \rangle \\ &= \left| \frac{1}{\omega_d^2 - \omega^2 - i\omega\gamma_d - 2\omega_d \mathbf{d} \cdot \mathbf{G}(\mathbf{r}_d, \mathbf{r}_d; \omega) \cdot \mathbf{d} / \hbar \epsilon_0} \right|^2, \end{aligned} \quad (17)$$

which contains important information about the local dot dynamics. Worth noting is that Eqs. (16) and (17) are applicable in any lossy, nonmagnetic inhomogeneous system, provided it is possible to calculate the Green function, which illustrates the strength of our technique. We also remark that it is relatively straightforward to include multiple QDs within this formalism.³⁴

Before closing this theory section, we make a few general comments on the form of the QD nonradiative decay rate γ_d . This broadening mechanism is likely caused by electron-phonon scattering and *pure dephasing*, which is especially important at elevated temperatures. Although we have not distinguished the mechanism of pure dephasing from an effective decay rate in the polarizability, the computed spectrum maintains precisely the same spectral shape for our chosen initial conditions;³⁵ so the distinction of pure dephasing (versus radiative broadening) is not necessary for computing the vacuum spectrum. However, if one knows the precise spectral form of the QD polarizability, including the influence of electron-phonon scattering, then only a small modification is needed in the above formulas.³⁵ For the calculations that follow below, we will adopt broadening values similar to colloidal dots at room temperature,³⁶ with $\gamma_d = 10$ – 20 meV. Note also that since the dominant decay is from nonradiative coupling to the lossy MNP, the details of the bare exciton decay are less important here (e.g., in comparison to coupling to a dielectric cavity system). An alternative quantum optics approach can include phonon interactions at the level of a polaron master equation.^{37,38}

III. RESULTS

A. Weak-coupling regime: Purcell factors and Lamb shifts

For our numerical calculations, we assume a MNP with a permittivity given by the Drude model, $\epsilon_m = \epsilon_\infty - \omega_m^2 / (\omega^2 - i\gamma_m \omega)$, and take the parameters typical for silver:⁷ $\epsilon_\infty = 6$, $\omega_m = 7.90$ eV, and $\gamma_m = 51$ meV; this gives an estimated $\gamma_{\text{LSP}} = 60$ meV and $\gamma_{\text{LSP}} = 75$ meV for 7- and 20-nm particles, respectively, in the regime where the dipole approximation is valid.

We consider a dipole emitter located $h = 2$ nm above a 7-nm and a 20-nm MNP. For the single-photon emitter (QD exciton), we consider both x -oriented and z -oriented dipoles with a dipole moment of $d = 24$ D ($\approx 0.5e$ nm), which is comparable to (or less than) the dipole moment used in other works that model QDs coupled to metals.^{7,18}

In Fig. 1(b) we show the LDOS versus height using both the nondipole and dipole calculations. We observe convergence between the solutions with the analytic and the dipole-approximation only for $h > 2a$, in agreement with Ref. 15. Additionally for the 20-nm radius MNP, we plot the same calculations performed using FDTD calculations³⁹ (squares and crosses) using a 1-nm grid and a 2-nm grid (finite-size emitters); we observe excellent agreement between these two different methods for both grid sizes.

In Figs. 2(a) and 2(d) we plot the LDOS as a function of frequency for $h = 2$ nm above the 7- and 20-nm MNPs for x -oriented and z -oriented dipoles, respectively. We immediately notice that the LDOS peaks are far separated in energy when compared to the dipole result, which is caused by the essential contribution from higher-order modes.⁴⁰ We also see that the LDOS peak for both nm-size particles is comparable, but the LDOS peak is slightly shifted between the two different sized particles. When comparing between x -oriented and z -oriented dipoles we see that the LDOS is larger for the latter case by about a factor of 2. Also note that the difference in

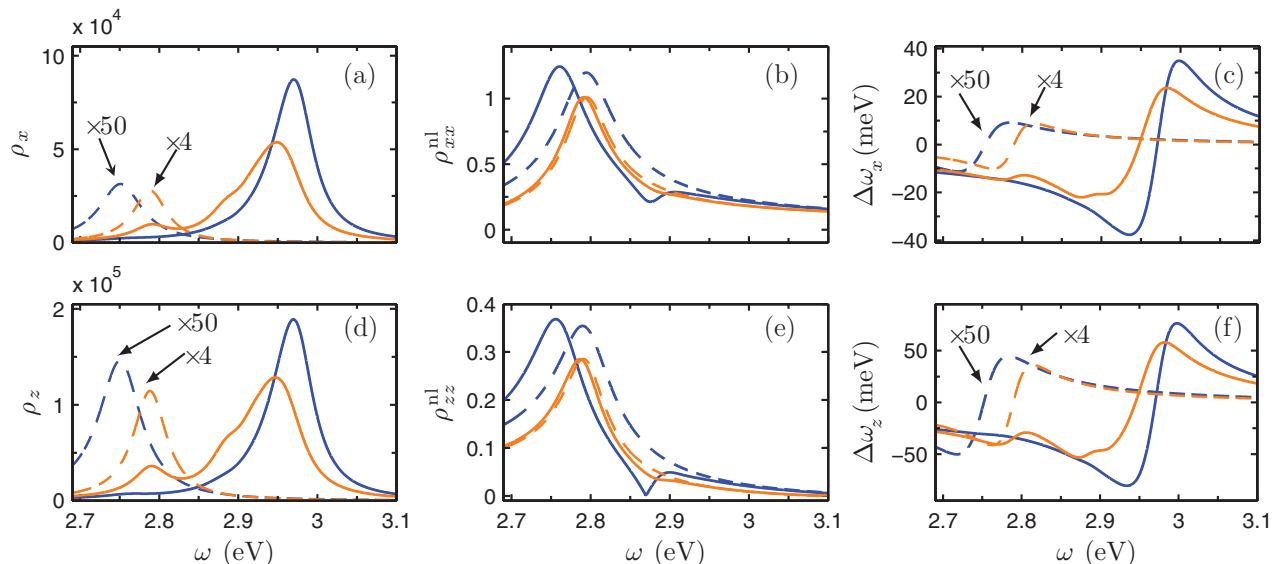


FIG. 2. (Color online) (a) LDOS versus frequency 2 nm above a 20-nm (blue-dark) and 7-nm (orange-light) silver MNP. The nondipole (exact) result is given by the solid line and the dipole-approximation result is given by the dashed line. (b) $\rho_{xx}^{nl}(\mathbf{r}_D, \mathbf{r}_d)$ versus frequency for $h_d = 2$ nm and $h_D = 1$ μ m, (c) Lamb shift versus frequency. In (a)–(c) we use an x -oriented emitter. (d)–(f) As (a)–(c) but for a z -oriented emitter. For clarity, dipole-approximation results are multiplied by a factor of 50 (20-nm particle) and 4 (7-nm particle) in graphs (a), (c) and (d), (f).

the dipole approximation for the 7-nm particle compared to the 20-nm particle is mainly due to the fact that they have different center-to-center distances; the shorter distance gives a larger result because of the scaling of the free space Green function in the near field, i.e., $\mathbf{G}_{\text{free}}(\mathbf{r}_d, \mathbf{r}_m) \propto |\mathbf{r}_d - \mathbf{r}_m|^{-3}$.

We next consider the nonlocal propagator in Figs. 2(b) and 2(e) for x -oriented and z -oriented emitters, respectively; this propagator is needed to account for light propagation from the dipole emitter to the detector. The detector is assumed to be at a height of 1 μ m above the MNP surface. For the 20-nm particle, the nondipole calculations for ρ^{nl} is spectrally peaked near $\omega \approx 2.76$ eV, which does not coincide with the peak of the LDOS (≈ 2.97 eV); however, the peak in the ρ^{nl} using a dipole approximation is shifted to 2.79 eV. We also observe an additional peak located near 2.9 eV, and we show below how this complex line shape affects the spontaneous emission spectrum. We can contrast these 20-nm MNP findings with the 7-nm results, where the ρ^{nl} in the dipole approximation agrees quite well with the exact result—although we begin to observe a small shoulder in the nondipole result, which indicates a second peak. Both nonlocal propagator peaks in this region are located at 2.8 eV, which is the same location as the dipole peaks seen in the LDOS and again the difference between x -oriented and z -oriented dipoles is about a factor of 2; but now the xx component of the nonlocal propagator is the larger (suggesting less quenching).

Figures 2(c) and 2(f) show the photonic Lamb shift for x -oriented and z -oriented dipoles, respectively, for both MNP sizes. Again the (invalid) dipole solutions are plotted for reference. The Lamb shifts at this height are quite large, giving a maximum frequency shift of $|\Delta\omega|_{\text{max}}/\omega = 7.9 \times 10^{-3}$ for the 7-nm particle and $|\Delta\omega|_{\text{max}}/\omega = 1.28 \times 10^{-2}$ for the 20-nm particle in the x direction, and a maximum frequency shift of $|\Delta\omega|_{\text{max}}/\omega = 2.02 \times 10^{-2}$ for the 7-nm particle and

$|\Delta\omega|_{\text{max}}/\omega = 2.75 \times 10^{-2}$ for the 20-nm particle in the z direction. For comparison, at $\omega \sim 3$ eV, an exciton linewidth of $\gamma_d \sim 15$ meV corresponds to $\gamma_d/\omega \approx 5 \times 10^{-3}$, so the largest frequency shift in Fig. 2(f) is more than five times the exciton linewidth (even at room temperature), which, to our knowledge, is much larger than any previously reported result. For photonic crystal systems,⁴¹ $|\Delta\omega|_{\text{max}}/\omega \approx 4 \times 10^{-5}$ has been reported, and for negative index metamaterial slabs,²⁶ $|\Delta\omega|_{\text{max}}/\omega \approx 5 \times 10^{-4}$ has been predicted.

B. Strong-coupling regime and emitted spectrum

Motivated by the significant enhancements seen in Fig. 2, we next study the nonperturbative strong-coupling regime, and calculate both the particle (or polarization) spectrum and the spontaneous emission spectrum of the field (Figs. 3 and 4). For all calculations we use $\gamma_d = 15$ meV, which corresponds to the decay of a typical QD exciton at room temperature.³⁶ Such a large decay would completely dominate semiconductor cavity systems, where the best (maximum) vacuum Rabi splittings are around 0.1–0.15 meV.⁴ For the 7-nm particle, with an x -oriented QD, the nondipole result (i.e., not treating the MNP as a dipole) for $P(\omega)$ [Fig. 3(a)] shows that there is a clear anticrossing, and the spectral location of strong coupling is evidently not located at the dipole LSP of 2.7915 eV; rather, it is much higher in energy at 2.9415 eV corresponding to the peak of the LDOS (~ 2.9489 eV). In contrast, the dipole result shows no indication of strong coupling. When looking at the far-field spectrum [see Fig. 3(c)], it is more difficult to observe an anticrossing as the weighting provided by ρ^{nl} causes the peaks to broaden and become more asymmetric. Additionally, there is a clear peak at 2.7885 eV, which corresponds to the peak in ρ^{nl} ; this spectral peak is not observable in the particle spectra; this additional peak also shows up when using

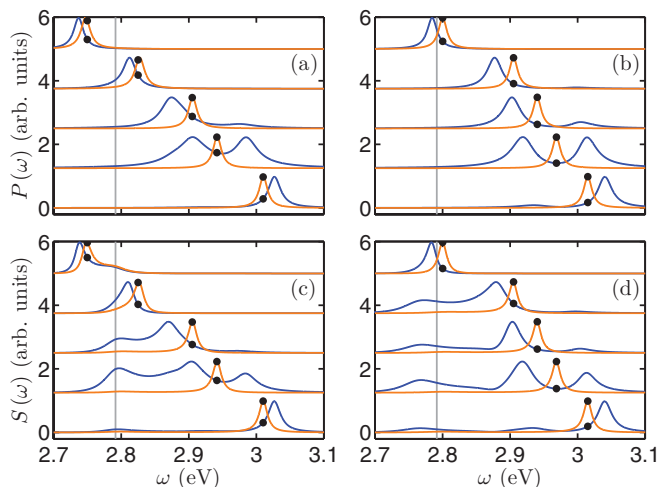


FIG. 3. (Color online) (a),(c) 7-nm particle [(b),(d) 20-nm particle] with an emitter 2 nm from the surface. Graphs (a),(b) and (c),(d) show the normalized effective particle and far-field spontaneous emission spectra, respectively, using the nondipole result (blue-dark line) and the dipole approximation (orange-light line) for an x -oriented dipole. Transition frequencies are indicated by black dots on the curves. The thin gray line in all graphs indicates the LSP resonance (at the maximum of α_m).

the dipole approximation but we emphasize that it is only due to photon propagation from the MNP/emitter system to the detector and is extremely small. We highlight that these additional spectral features in the emission spectrum are quite different to a dielectric cavity system.

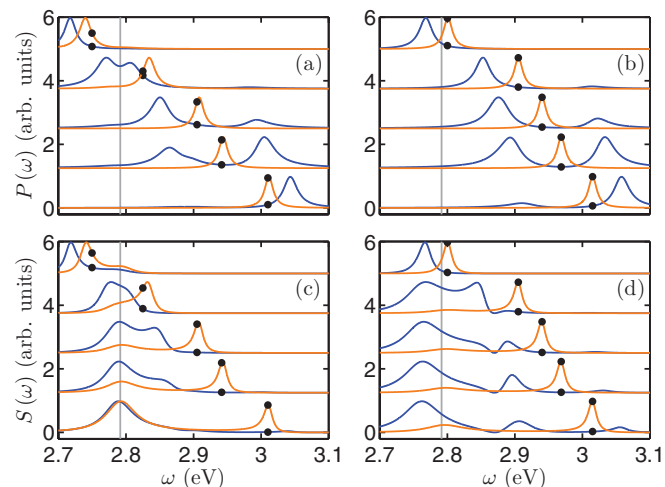


FIG. 4. (Color online) As in Fig. 3, but with a z -oriented QD dipole.

From the calculations above, it is also clear that the predicted Lamb shifts are observable in the spectra as the exciton spectral peaks in both the particle and the far-field spectra are substantially shifted in energy. Figures 3(b) and 3(d) show the particle and light spectra for the 20-nm MNP, and we observe many similar features to the 7-nm spectra; however, the splitting between the peaks in the particle spectrum is notably larger for the 20-nm particle compared to the 7-nm particle. In the far-field spectra, we also see that there are significant qualitative differences as the QD frequency is tuned, though the anticrossing region is observed at similar

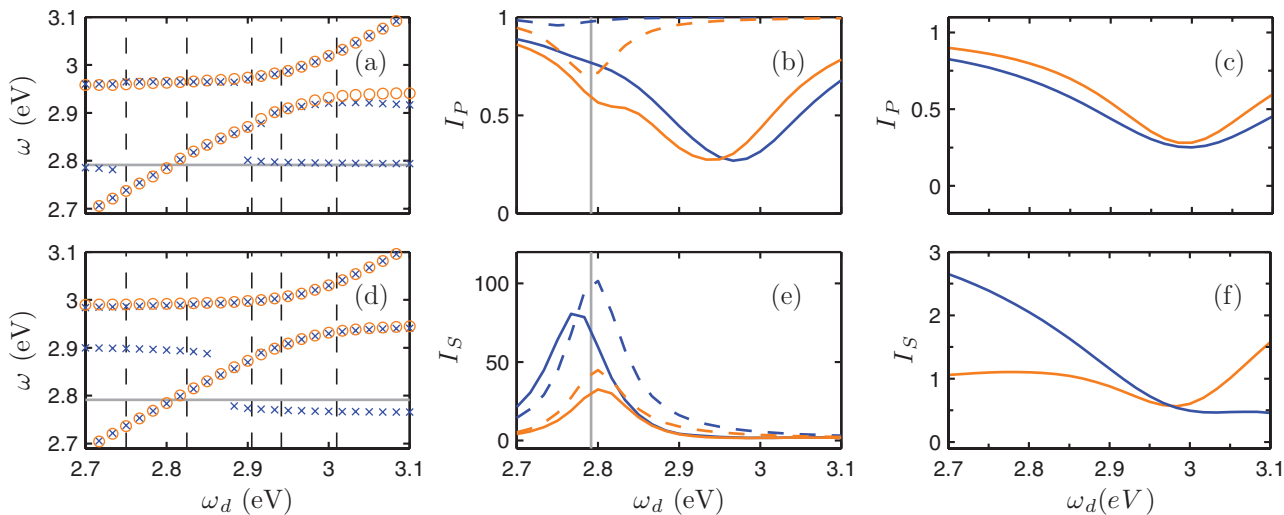


FIG. 5. (Color online) (a) 7-nm particle [(d) 20-nm particle] with an emitter 2 nm from the surface tracking the particle spectral peaks (orange circles) and light emission spectral peaks (blue crosses) as a function of QD frequency for an x -oriented QD. The dashed lines correspond to the location of the QD transition frequencies used in the graphs in Fig. 3. (b) Integrated particle spectra for an x -oriented QD normalized by the integrated particle spectrum without the MNP (i.e., free space) as a function of QD transition frequency for 20-nm MNP (blue-dark line) and 7-nm MNP (orange-light line) for dipole (dashed line) and nondipole (solid line) calculations. (c) Integrated particle spectrum 2 nm above a metallic half space normalized by integrated particle spectrum in free space as a function of QD transition frequency for z -oriented QD (blue-dark line) and x -oriented QD (orange-light line). (e) As (b) but with the integrated far-field spectrum normalized by the integrated far-field spectrum without the MNP. (f) As (c) but with the integrated far-field spectrum normalized by the integrated far-field spectrum in free space. The thin gray lines in (a), (b), (d), and (e) indicate the LSP resonance.

QD detunings. This shows that the strong coupling is clearly an observable effect, even with significant metal losses.

Figure 4 shows similar results to those shown in Fig. 3, but with a z -oriented exciton. The larger LDOS for this polarization manifests in an increased Rabi splitting in both particle and far-field spectra, however, the peaks at higher energies are more difficult to observe on this scale due to the smaller value of the nonlocal propagator in the higher frequency range [see Fig. 2(e)].

To further examine the anticrossing behavior of strong coupling, we have located the maxima in the particle spectra (red circles) and far-field spectra (blue crosses) for various QD transition frequencies, and show these in Fig. 5(a) for 7-nm particles, and Fig. 5(d) for 20-nm particles using an x -oriented QD (similar results are found for a z -oriented dipole). In both the particle and light emission spectra, a clear anticrossing is observable, indicating a vacuum Rabi splitting of around $2g \approx 79$ meV for 7-nm particles and $2g \approx 95$ meV for 20-nm particles; note that $2g > 120$ meV for both sizes of MNP for the z -oriented QD (not shown). Clearly this observation does not correspond to the location of the lowest-order dipole mode (indicated by the thin gray lines in Fig. 3) but is due to the coupling to higher-order plasmon modes. For the emitted light spectrum, the effects of propagation add additional peaks; however, the vacuum Rabi splitting is well maintained even with nonradiative quenching. This finding is not at all clear unless one properly accounts for propagation to the detector.

In Figs. 5(a) and 5(d) we discern an additional peak in the far field at the location of the dipole mode, which is due to light propagation (via ρ^{nl}), and in Fig. 5(d) there is a fourth peak, which is due to the dip located in ρ^{nl} that only occurs for the 20-nm particle, but becomes too small to resolve after $\omega_d \approx 2.85$ eV. These spontaneous emission spectra contain highly non-Lorentzian line shapes as well as essential nondipolar interaction effects. Furthermore, any predictions of strong coupling with MNPs must include higher-order mode coupling as they will dominate the dynamics before it is ever possible to achieve strong coupling using the dipole mode (at least for our chosen parameters).

Finally, we study the optical quenching effects in more detail. In Figs. 5(b) and 5(e) we calculate the integration of the particle/far-field spectrum as a function of ω_d , and we normalize this to the integrated free-space value. We define the integrated spectral quantities $I_P(\omega_d)$ (integrated particle spectrum) or $I_S(\omega_d)$ (integrated far-field spectrum), which are computed as follows:

$$I_P(\omega_d) = \frac{\int_0^\infty P(\omega, \omega_d) d\omega}{\int_0^\infty P_{\text{hom}}(\omega, \omega_d) d\omega}, \quad (18)$$

$$I_S(\omega_d) = \frac{\int_0^\infty S(\omega, \omega_d) d\omega}{\int_0^\infty S_{\text{hom}}(\omega, \omega_d) d\omega}. \quad (19)$$

These integrals give the likelihood of detecting a photon emitted by a QD, and the values in the vicinity of the MNP are normalized to the values that would be obtained from a QD in vacuum (for this particular particle/detector geometry). We show MNP dipole-approximation (dashed) and nondipole (solid) results for a 7-nm MNP (orange-light line) and a 20-nm MNP (blue-dark line). For the integrated particle spectra I_P

we see that, in terms of emitted flux, quenching is much more problematic for the nondipolar result compared to the dipolar result. The region of greatest quenching is where the LDOS is peaked giving a maximum reduction to $I_P \approx 0.3$ in the region of the anticrossing. Such an observation would lead one to believe that MNPs appear to absorb the majority of the emitted photons. However, in the far-field spectrum I_S , we see a dramatic *increase* in the relative number of photons detected for QDs located near the LSP of 30 (80) for 7 nm (20 nm). Even in the anticrossing region, the enhancement is $\approx 2-3$ compared to a QD in free space. This enhancement in the integrated far-field spectrum shows that even in the frequency region where photons appear to be dominated by nonradiative effects, the MNP compensates by acting as an antenna making the detection of far-field radiation more efficient.

To help further clarify the physics of metallic quenching, we also compare the MNP case with a metallic half space, where we calculate the Green function using a well-known multilayer scattering technique.^{26,42} We initially verify in Fig. 5(c) that a simple metallic half space suffers similar quenching to the MNP in the particle spectrum; however, it feels much more quenching in the far-field spectrum [Fig. 5(f)] with I_S lower by about two orders of magnitude for both z -oriented (blue-dark line) and x -oriented (orange-light line) QDs. It is worth noting that the reduction of γ_d to values typical for QDs at cryogenic temperatures ($\approx \mu\text{eV}$) results in significantly more quenching in both the particle spectrum and the far-field spectrum for QDs coupled to MNPs; for example, using $\gamma_d < 50\text{-}\mu\text{eV}$ results in $I_S < 1$ over the entire frequency range showing that the antenna effect of the MNP is unable to overcome the quenching in the case of sharp QD linewidths.

For these quantum optical studies above, we have deliberately chosen a rather large dipole moment ($d = 24$ D) to enable the strong-coupling regime. For smaller dipole sizes, e.g., with $d = 12$ D for the x -oriented dipole, or $d = 8$ D for a z -oriented dipole, we obtain qualitatively similar strong-coupling results but with smaller vacuum Rabi splittings. There is also the potential to see strong coupling with even lower QD dipole moments, if one uses MNPs with nonspherical shapes, e.g., cigar shapes.¹⁸ For much lower dipole moments then the strong-coupling effect of course vanishes, although dimer^{7,43} configurations may help to increase the LDOS to a sufficiently larger value.

IV. DISCUSSION

We now briefly discuss some potential experimental configurations for observing the effects presented above. There are several possible experimental scenarios that are likely within reach of current nanofabrication techniques.⁴⁴ One example could involve spin coating colloidal QDs onto a substrate, locating the dots by correlating photoluminescence data with atomic force microscopy (AFM) images and positioning the MNPs in the vicinity of the QD using the AFM tip as was done by Ratchford *et al.*;⁶ in their study, the relatively small QDs had an estimated dipole moment of around 5.3 D and a strong modification of the spontaneous emission rate was shown, along with a drastic reduction in blinking. A second

possible method for probing the emission spectra of coupled QD-MNP systems could use an array of MNPs placed on a substrate and immersed in a solution of colloidal QDs. By illuminating with focused (off-resonant) laser beams it is also possible to create efficient optical traps^{45–47} at which point the QD can be loaded into an excited state. Both of these proposals involve the use of substrates; of note, our formalism enables the calculation of the far-field spectrum in any inhomogeneous geometry as long as the Green function can be calculated; our initial results using the FDTD technique [see Fig. 1(b)] for this simplified geometry can easily include a substrate; or even more complicated geometries could be investigated such as MNPs coupled directly to photonic crystal cavities containing QDs.^{44,48} In fact, recent experiments with QDs coupled with disordered metallic films on glass substrates are at a loss for the expected far-field emission spectra,⁴⁹ further emphasizing the usefulness of our technique.

V. CONCLUSIONS

We have presented a Green-function quantum optics approach to study quantum optical interactions between a QD photon emitter and a single (finite-size) MNP. We began by examining the properties of the classical Green function above a MNP within and beyond the dipole approximation and showed the dramatic effects of the higher-order plasmon modes on the LDOS and photonic Lamb shifts. Going beyond the weak-coupling approximation, we then examined the particle spectrum and contrasted this with the far-field (observable) light-emission spectrum of a QD strongly-coupled to the MNP. Using experimentally accessible parameters, our nonperturbative light spectra show clear signatures of the

strong-coupling regime; the emitted spectrum was found to contain a triplet or quartet of resonances, highlighting the important role of light propagation to the detector. Finally, we also examined the role of optical quenching on the far-field spectra, and compared the quenching to the case of a metal half space. It should be emphasized that our presented techniques are quite general and can be extended to include an initial pump field, multiple MNPs, and multiple QDs.

ACKNOWLEDGMENTS

This work was supported by the Natural Sciences and Engineering Research Council of Canada (NSERC) and The Danish Council for Independent Research (Grant No. FTP 10-093651).

APPENDIX: SPHERICAL GREEN FUNCTION

Given a sphere with permittivity ϵ_m and radius a , embedded in a homogeneous medium of permittivity ϵ_b , the scattered part of the Green function is given by

$$\mathbf{G}^{\text{scatt}}(\mathbf{r}, \mathbf{r}') = \frac{-ik_b}{4\pi} \sum_{e,o} \sum_{n=1}^{\infty} \sum_{m=0}^n (2 - \delta_m^0) \frac{2n+1}{n(n+1)} \frac{(n-m)!}{(n+m)!} \times [R^H \mathbf{M}_{mn}^{eo}(k_b \mathbf{r}) \mathbf{M}_{mn}^{eo}(k_b \mathbf{r}') + R^V \mathbf{N}_{mn}^{eo}(k_b \mathbf{r}) \mathbf{N}_{mn}^{eo}(k_b \mathbf{r}')], \quad (\text{A1})$$

where R_H/R_V are the centrifugal reflection coefficients corresponding to transverse electric/magnetic waves (TE/TM), and $\mathbf{M}_{mn}^{eo}/\mathbf{N}_{mn}^{eo}$ are the vector functions corresponding to TE/TM waves and they have been separated into even and odd contributions. The values of R_H, R_V , are given by

$$R^H = \frac{k_m \partial \tau_m \tau_b - k_b \partial \tau_b \tau_m}{k_m \partial \tau_m \kappa_b - k_b \partial \kappa_b \tau_m}, \quad R^V = \frac{k_m \tau_m \partial \tau_b - k_b \tau_b \partial \tau_m}{k_m \tau_m \partial \kappa_b - k_b \kappa_b \partial \tau_m}, \quad (\text{A2})$$

where

$$\tau_i = j_n(k_i a), \quad \kappa_i = h_n^{(1)}(k_i a), \quad (\text{A3})$$

$$\partial \tau_i = \frac{1}{k_i a} \frac{\partial [k_i a j_n(k_i a)]}{\partial k_i a}, \quad \partial \kappa_i = \frac{1}{k_i a} \frac{\partial [k_i a h_n^{(1)}(k_i a)]}{\partial k_i a}. \quad (\text{A4})$$

Here $j_n, h_n^{(1)}$ are the spherical Bessel functions and spherical Hankel functions of the first kind, respectively and $k_i = \omega \sqrt{\epsilon_i}/x$ where i corresponds to either the metal or background. The vector functions are defined as follows:

$$\mathbf{M}_{mn}^e(k\mathbf{r}) = -\frac{m}{\sin \theta} h^{(1)}(kr) P_n^m(\cos \theta) \sin m\phi \hat{\theta} - h^{(1)}(kr) \frac{dP_n^m(\cos \theta)}{d\theta} \cos m\phi \hat{\phi}, \quad (\text{A5})$$

$$\mathbf{M}_{mn}^o(k\mathbf{r}) = \frac{m}{\sin \theta} h^{(1)}(kr) P_n^m(\cos \theta) \cos m\phi \hat{\theta} - h^{(1)}(kr) \frac{dP_n^m(\cos \theta)}{d\theta} \sin m\phi \hat{\phi}, \quad (\text{A6})$$

$$\mathbf{N}_{mn}^e(k\mathbf{r}) = \frac{n(n+1)}{kr} h^{(1)}(kr) P_n^m(\cos \theta) \cos m\phi \hat{r} + \frac{1}{kr} \frac{d[rh^{(1)}(kr)]}{dr} \left[\frac{dP_n^m(\cos \theta)}{d\theta} \cos m\phi \hat{\theta} - \frac{m}{\sin \theta} P_n^m(\cos \theta) \sin m\phi \hat{\phi} \right], \quad (\text{A7})$$

$$\mathbf{N}_{mn}^o(k\mathbf{r}) = \frac{n(n+1)}{kr} h^{(1)}(kr) P_n^m(\cos \theta) \sin m\phi \hat{r} + \frac{1}{kr} \frac{d[rh^{(1)}(kr)]}{dr} \left[\frac{dP_n^m(\cos \theta)}{d\theta} \sin m\phi \hat{\theta} + \frac{m}{\sin \theta} P_n^m(\cos \theta) \cos m\phi \hat{\phi} \right]. \quad (\text{A8})$$

where P_n^m are Legendre polynomials. Note that for our numerical calculation in this paper, a few simplifying assumptions can be made; we only consider the calculation to be along the z direction, $x = x' = y = y' = 0$, and we additionally assume that we

are only calculating the LDOS ($z = z'$). This means that calculating in the $\hat{\theta}\hat{\theta}$ direction is equivalent to the $\hat{\phi}\hat{\phi}$ direction. This allows us to simplify Eqs. (A5)–(A8) to

$$\mathbf{M}_{mn}^e(k\mathbf{r}) = h^{(1)}(kr) \frac{dP_n^m(0)}{d\theta} \hat{\phi}, \quad (\text{A9})$$

$$\mathbf{M}_{mn}^o(k\mathbf{r}) = 0, \quad (\text{A10})$$

$$\mathbf{N}_{mn}^e(k\mathbf{r}) = \frac{n(n+1)}{kr} h^{(1)}(kr) P_n^m(0) \hat{r}, \quad (\text{A11})$$

$$\mathbf{N}_{mn}^o(k\mathbf{r}) = \frac{m}{kr} \frac{d[rh^{(1)}(kr)]}{dr} P_n^m(0) \hat{\phi}. \quad (\text{A12})$$

*cvanvlack@physics.queensu.ca

- ¹K. J. Vahala, *Nature (London)* **424**, 839 (2003).
- ²E. M. Purcell, *Phys. Rev.* **69**, 681 (1946).
- ³Y. Akahane, T. Asano, B.-S. Song, and S. Noda, *Nature (London)* **425**, 944 (2003).
- ⁴J. P. Reithmaier, G. Sek, A. Löffler, C. Hofmann, S. Kuhn, S. Reitzenstein, L. V. Keldysh, V. D. Kulakovskii, T. L. Reinecke, and A. Forchel, *Nature (London)* **432**, 197 (2004).
- ⁵S. A. Maier, *Plasmonics: Fundamentals and Applications* (Springer, US, 2007).
- ⁶D. Ratchford, F. Shafiei, S. Kim, S. K. Gray, and X. Li, *Nano Lett.* **11**, 1049 (2011).
- ⁷S. Savasta, R. Saija, A. Ridolfo, O. Di Stefano, P. Denti, and F. Borghese, *ACS Nano* **4**, 6369 (2010).
- ⁸L.-M. Duan and H. J. Kimble, *Phys. Rev. Lett.* **92**, 127902 (2004).
- ⁹C. Monroe, *Nature (London)* **416**, 238 (2002).
- ¹⁰D. J. Bergman and M. I. Stockman, *Phys. Rev. Lett.* **90**, 027402 (2003).
- ¹¹M. A. Noginov, G. Zhu, A. M. Belgrave, R. Bakker, V. M. Shalaev, E. E. Narimanov, S. Stout, E. Herz, T. Suteewong, and U. Wiesner, *Nature (London)* **460**, 1110 (2009).
- ¹²N. I. Zheludev, S. L. Prosvirnin, N. Papisimakis, and V. A. Fedotov, *Nat. Photon.* **2**, 351 (2008).
- ¹³E. Waks and D. Sridharan, *Phys. Rev. A* **82**, 043845 (2010).
- ¹⁴R. Carminati, J.-J. Greffet, C. Henkel, and J. Vigoureux, *Opt. Commun.* **261**, 368 (2006).
- ¹⁵E. Castanić, M. Boffety, and R. Carminati, *Opt. Lett.* **35**, 291 (2010).
- ¹⁶P. Anger, P. Bharadwaj, and L. Novotny, *Phys. Rev. Lett.* **96**, 113002 (2006).
- ¹⁷R. Ruppin, *J. Chem. Phys.* **76**, 1681 (1982).
- ¹⁸A. Trügler and U. Hohenester, *Phys. Rev. B* **77**, 115403 (2008).
- ¹⁹U. Hohenester and A. Trügler, *IEEE J. Sel. Top. Quantum Electron.* **14**, 1430 (2008).
- ²⁰H. J. Carmichael, *Statistical Methods in Quantum Optics I* (Springer-Verlag, Berlin, 1999).
- ²¹C.-T. Tai, in *Dyadic Green's Functions in Electromagnetic Theory*, edited by D. K. Cheng (Intext Educational Publishers, Scranton, PA, 1971).
- ²²L.-W. Li, P.-S. Kooi, M.-S. Leong, and T.-S. Yeo, *IEEE Trans. Microwave Theor. Tech.* **42**, 2302 (1994).
- ²³B. Draine, *Astrophys. J.* **333**, 848 (1988).
- ²⁴J.-J. Greffet, M. Laroche, and F. Marquier, *Phys. Rev. Lett.* **105**, 117701 (2010).
- ²⁵L. Novotny and B. Hecht, *Principles of Nano-Optics* (Cambridge University, Cambridge, England, 2006).
- ²⁶P. Yao, C. Van Vlack, A. Reza, M. Patterson, M. M. Dignam, and S. Hughes, *Phys. Rev. B* **80**, 195106 (2009).
- ²⁷H. T. Dung, L. Knöll, and D.-G. Welsch, *Phys. Rev. A* **57**, 3931 (1998).
- ²⁸H. T. Dung, S. Y. Buhmann, L. Knöll, D. G. Welsch, S. Scheel, and J. Kästel, *Phys. Rev. A* **68**, 043816 (2003).
- ²⁹W. Vogel and G. Welsch, *Quantum Optics* (Wiley-VCH, Weinheim, 2006).
- ³⁰S. Stobbe, P. T. Kristensen, J. E. Mortensen, J. M. Hvam, J. Mørk, and P. Lodahl, e-print [arXiv:1112.1835v1](https://arxiv.org/abs/1112.1835v1).
- ³¹K. J. Ahn and A. Knorr, *Phys. Rev. B* **68**, 161307 (2003).
- ³²P. C. Chaumet, A. Sentenac, and A. Rahmani, *Phys. Rev. E* **70**, 036606 (2004).
- ³³J. R. Zurita-Sánchez and L. Novotny, *J. Opt. Soc. Am. B* **19**, 1355 (2002).
- ³⁴P. T. Kristensen, J. Mørk, P. Lodahl, and S. Hughes, *Phys. Rev. B* **83**, 075305 (2011).
- ³⁵S. Hughes, P. Yao, F. Milde, A. Knorr, D. Dalacu, K. Mnaymneh, V. Sazonova, P. J. Poole, G. C. Aers, J. Lapointe, R. Cheriton, and R. L. Williams, *Phys. Rev. B* **83**, 165313 (2011).
- ³⁶H. Qiao, K. A. Abel, F. C. J. M. van Veggel, and J. F. Young, *Phys. Rev. B* **82**, 165435 (2010).
- ³⁷C. Roy and S. Hughes, *Phys. Rev. Lett.* **106**, 247403 (2011).
- ³⁸I. Wilson-Rae and A. Imamoğlu, *Phys. Rev. B* **65**, 235311 (2002).
- ³⁹We use Lumerical's FDTD Solutions: [www.lumerical.com].
- ⁴⁰G. Sun and J. B. Khurgin, *Appl. Phys. Lett.* **97**, 263110 (2010).
- ⁴¹X.-H. Wang, Y. S. Kivshar, and B.-Y. Gu, *Phys. Rev. Lett.* **93**, 073901 (2004).
- ⁴²M. Paulus, P. Gay-Balmaz, and O. J. F. Martin, *Phys. Rev. E* **62**, 5797 (2000).
- ⁴³A. F. Koenderink, *Opt. Lett.* **35**, 4208 (2010).
- ⁴⁴O. Benson, *Nature (London)* **480**, 193 (2011).
- ⁴⁵A. N. Grigorenko, N. W. Roberts, M. R. Dickinson, and Y. Zhang, *Nat. Photon.* **2**, 365 (2008).
- ⁴⁶D. E. Chang, J. D. Thompson, H. Park, V. Vuletić, A. S. Zibrov, P. Zoller, and M. D. Lukin, *Phys. Rev. Lett.* **103**, 123004 (2009).
- ⁴⁷M. Righini, A. S. Zelenina, C. Girard, and R. Quidant, *Nat. Phys.* **3**, 477 (2007).
- ⁴⁸M. Barth, S. Schietinger, S. Fischer, J. Becker, N. Nüsse, T. Aichele, B. Löchel, C. Sönnichsen, and O. Benson, *Nano. Lett.* **10**, 891 (2010).
- ⁴⁹D. Canneson, I. Mallek-Zouari, S. Buil, X. Quélin, C. Javaux, B. Mahler, B. Dubertret, and J.-P. Hermier, *Phys. Rev. B* **84**, 245423 (2011).